

# Limitations of emittance and source size measurement of laser-accelerated electron beams using the pepper-pot mask method

F. C. Salgado,<sup>1,2,3,\*</sup> A. Kozan,<sup>1,2,3</sup> D. Seipt,<sup>1,2,3</sup> D. Hollatz,<sup>1,2,3</sup> P. Hilz,<sup>1,2,3</sup>  
M. Kaluza,<sup>1,2,3</sup> A. Sävert,<sup>1,2,3</sup> A. Seidel,<sup>1,2,3</sup> D. Ullmann,<sup>1,2,3</sup> Y. Zhao,<sup>1,2,3</sup> and M. Zepf<sup>1,2,3</sup>

<sup>1</sup>*Institute of Optics and Quantum Electronics, Friedrich-Schiller-Universität, Max-Wien-Platz 1, 07743 Jena, Germany*

<sup>2</sup>*Helmholtz-Institut Jena, Fröbelstieg 3, 07743 Jena, Germany*

<sup>3</sup>*GSI Helmholtzzentrum für Schwerionenforschung, Planckstraße 1, 64291 Darmstadt, Germany*

(Dated: December 16, 2024)

The pepper-pot method is a widely used technique originally proposed for measuring the emittance of space-charge-dominated electron beams from radio-frequency photoinjectors. With recent advances in producing high-brightness electron beams via laser wakefield acceleration (LWFA), the method has also been applied to evaluate emittance in this new regime [1–3]. In this work, we explore the limitations of the method in inferring the emittance and beam waist of LWFA electron beams, showing that the technique becomes inaccurate for small emittance values.

## I. INTRODUCTION

Small source sizes and high-quality beams are required to drive the new generation of light sources, such as free-electron lasers (FELs) [4–7], electron-positron particle colliders [8–11], and Thomson sources [12, 13]. An attractive alternative to conventional radio-frequency (RF) accelerators for producing the required high-quality beams is the laser wakefield acceleration (LWFA) technique [14]. The laser wakefield accelerator generates longitudinal electric gradient fields approximately three orders of magnitude larger than conventional RF accelerators. This capability enables the generation of GeV beams while significantly reducing the footprint of the machines compared to linear accelerators.

The quality of electron beams is defined by the brightness parameter  $\mathcal{B}_n$ , which is a function of the beam current  $I$  and its transverse normalized emittance  $\epsilon_n$  in the  $x$  and  $y$  directions, as described in Ref. [15]:

$$\mathcal{B}_n \propto \frac{I}{\epsilon_{n_x} \epsilon_{n_y}}. \quad (1)$$

To achieve a high-brightness beam, one can either increase the beam current  $I$  or decrease the emittance of the particle beam. In this study, we specifically focus on the transverse emittance parameter, a critical property of the beam describing how well the particles are confined within its transverse phase space. High-brightness beams can be achieved by methods such as laser-wakefield acceleration (LWFA) or plasma-photocathodes which exhibit brightness above  $10^{17}$  A/m<sup>2</sup>/0.1% [16, 17]. Therefore, accurate methods to measure the emittance of a beam are required to correctly determine the brightness of a particle beam.

Various methods have been used to characterize the transverse emittance of electron beams in the order of a few- mmrad, for example, quadrupole and solenoid

scans [18–20], transverse deflecting structures (TDS) [21–27], Shintake monitors [28, 29] and laser gratings [30, 31]. These methods rely on adding new components to the beamline, such as extra magnets and focusing optics, which increase the footprint of the diagnostics used, or they involve scanning methods. However, the pepper-pot mask method has been widely used as an alternative method to evaluate the emittance of LWFA beams due to its simplicity in assembling the diagnostic by only adding a single pepper-pot mask of a few square millimeters in size in the beam path of the experiment [1–3, 32, 33]. To understand the pepper-pot method in detail, we focus in this work on investigating its properties in diagnosing the emittance of laser-accelerated electron beams and how accurately the diagnostic can infer the beam’s transverse emittance and waist.

Initially, the pepper pot (PP) method was primarily designed and extensively utilized to characterize the phase space of radio-frequency photoinjectors. These photoinjectors typically feature electron beams with only a few-MeV energy and a large beam waist, resulting in low divergence [34–37]. Such beams are often characterized by space charge effects. However, recently, the PP method has been widely used to characterize the emittance of LWFA beams due to its simplicity, despite the fact that LWFA beams are emittance-dominated.

The propagation of an electron beam can be characterized as either space charge-dominated or emittance-dominated. To classify the regime in which the electron beam operates, we can compare the terms of the root mean square (rms) beam envelope equation in a drift space [15, 36, 37],

$$\sigma_x'' = \frac{\epsilon_n^2}{\gamma^2 \sigma_x} + \frac{I}{\gamma^3 I_0 (\sigma_x + \sigma_y)}, \quad (2)$$

where  $I$  is the peak beam current,  $I_0 = 17$  kA is the Alfvén current,  $\epsilon_n$  is the normalized emittance of the beam, and  $\sigma_x$  and  $\sigma_y$  are the rms beam waist, also known as the source sizes, in the  $x$ - and  $y$ -directions.

By taking the ratio  $\mathcal{R}$  of the two terms on the right-hand side of Eq. (2), and assuming a round beam, i.e.,

\* felipe.salgado@uni-jena.de

$\sigma_0 = \sigma_x = \sigma_y$ , we obtain [36],

$$\mathcal{R} = \frac{I \sigma_0}{2 I_0 \gamma \epsilon_n^2}, \quad (3)$$

A beam is said to be space-charge dominated when its ratio  $\mathcal{R} \gg 1$ . Beams generated by RF-photoinjectors, for example, easily fall into this category due to their divergence of a few-mrad, energy of about 5 MeV, and typical rms waist sizes of approximately 0.5 mm [38]. In contrast, LWFA electron beams [39, 40] can achieve higher energies in the order of 100's of MeV and beyond at the output of the first stage, with much smaller beam waists on the order of a few  $\mu\text{m}$  while maintaining their divergence similar to radio-frequency accelerated beams of few-mrad. This combination of parameters leads LWFA beams to have an  $\mathcal{R} \approx 0.07 \ll 1$ , indicating that they are emittance dominated, i.e., the particles are well confined within their transverse phase space during propagation (assuming a monoenergetic beam).

In this study, we investigate the range of applicability of the pepper-pot technique in inferring the emittance of LWFA electron beams.

## II. THEORY

In this section, we briefly introduce the definition of beam emittance and later the theory that underlies the method used to estimate the rms emittance using pepper-pot masks.

### A. Beam emittance

The emittance of a beam is defined as its volume occupied in phase space. For a monoenergetic beam without accelerating forces acting upon it, the emittance remains constant during its propagation (assuming ideal magnets and quadrupoles and neglecting radiation reaction).

In the two-dimensional case, which is the focus of this work, the equation of the phase space ellipse can be expressed in terms of the particle's coordinate vector  $\mathbf{u} = (x, x')$ , such that  $\mathbf{u}^T \boldsymbol{\sigma}^{-1} \mathbf{u} = 1$ , where  $x$  represents the particle's position,  $x'$  denotes the divergence, and  $\boldsymbol{\sigma}$  is the symmetric beam matrix,

$$\boldsymbol{\sigma} = \begin{pmatrix} \sigma_{11} & \sigma_{12} \\ \sigma_{12} & \sigma_{22} \end{pmatrix}. \quad (4)$$

The area is bounded by the density distribution of the particles  $\rho(x, x') = \rho(\mathbf{u}^T \boldsymbol{\sigma}^{-1} \mathbf{u})$  assuming a Gaussian distribution,

$$\rho(x, x') \propto \exp \left[ -\frac{(\sigma_{22} x^2 - 2\sigma_{12} x x' + \sigma_{11} x'^2)}{2 \det \boldsymbol{\sigma}} \right]. \quad (5)$$

The  $1/\pi$  area occupied by the distribution given in Eq. (5), i.e., the root mean square (rms) emittance of

the electron beam, is then defined as

$$\epsilon_{\text{rms}}^2 = \det \boldsymbol{\sigma} = \langle x^2 \rangle \langle x'^2 \rangle - \langle x x' \rangle^2 \approx \sigma_x^2 \theta_x^2. \quad (6)$$

The notation  $\langle \cdot \rangle$  represents the second moment of the quantity within the brackets and is directly correlated with the beam matrix as  $\sigma_{11} = \langle x^2 \rangle = \sigma_x^2$ ,  $\sigma_{22} = \langle x'^2 \rangle = \theta_x^2$ , and  $\sigma_{12} = \langle x x' \rangle$ . For details on how the terms correlate with each other, please see Ref. [15, 41]. An ideal beam, i.e., a perfectly monoenergetic beam with all particles propagating in the same direction, will occupy the same momentum in its phase space and, consequently, have a null emittance.

The area of the beam phase space is approximately the product of the rms source size  $\sigma_x$  of the beam in its waist, and its divergence  $\theta_x$  as shown in Eq. (6). Hence, by measuring the geometric emittance of a beam and its divergence, it is possible to estimate its source size. The subscript  $x$  represents the axis in which the beam waist and divergence are measured, in this case, in the horizontal direction (x-direction). The electron beam propagates along the z-axis.

A broadband particle beam is composed of particles with different energies and, consequently, the rms emittance given in Eq. (6) does not remain constant throughout the propagation of the beam due to the various rotation velocities in phase space of the particles with different energies. To account for such effects, one can remove the effects of the different rotation speeds of the phase space ellipse and normalize the equation with respect to the energy of the particles within the beam, here represented by the average Lorentz-factor  $\langle \gamma \rangle$  of the particle. The normalized emittance  $\epsilon_n$  is then evaluated as [42]

$$\epsilon_n^2 = \langle \gamma \rangle^2 \left[ \left( \frac{\sigma_E}{E} \right)^2 \langle x^2 \rangle \langle x'^2 \rangle + \epsilon_{\text{rms}}^2 \right], \quad (7)$$

where the term  $\sigma_E/E$  is the energy spread of the beam given as

$$\left( \frac{\sigma_E}{E} \right)^2 = \frac{\langle \beta^2 \gamma^2 \rangle - \langle \beta \gamma \rangle^2}{\langle \gamma \rangle^2}. \quad (8)$$

While propagating inside the plasma channel, an LWFA electron beam experiences strong focusing forces that keep its beam waist very small while inducing a significant angular spread [14]. As the beam approaches the plasma-vacuum interface, a density transition occurs over a few hundred micrometers, which weakens the focusing forces. This results in an increase in the beam waist but a decrease in its divergence, thereby preserving the beam emittance [2, 18]. At the plasma exit, the beam envelope is assumed to be at its waist, with its transverse size increasing due to free expansion during its subsequent drift [42]. Assuming a sufficiently long propagation length in vacuum after the beam exits the plasma, one can express Eq. (7) in terms of the drift length  $L_{\text{drift}}$ , as demonstrated in previous studies [42, 43]:

$$\epsilon_n^2 = \langle \gamma \rangle^2 \left[ \left( \frac{\sigma_E}{E} \right)^2 \theta_x^4 L_{\text{drift}}^2 + \epsilon_{\text{rms}}^2 \right]. \quad (9)$$

## B. The pepper-pot mask technique

The pepper-pot method was initially developed to diagnose space charge-dominated beams by transforming the beam into beamlets that possess sufficient charge but are not significantly defocused due to space charge effects, i.e., emittance-dominated beamlets. The pepper-pot is a mask made of a high-density material with a grid of holes or slits perpendicular to the propagation axis of the electron beam. This mask samples the test electron beam into smaller, emittance-dominated beamlets, which then propagate toward a scintillation screen positioned downstream of the mask. The screen is imaged by a high-resolution imaging system and the emittance of the electron beam is determined by evaluating the size of the beamlets and their positions according to the mathematical description introduced by Ref. [44]. In this section, we briefly introduce the method we used to reconstruct and retrieve the root mean square (rms) emittance of the test electron beams utilizing pepper-pot masks.

### 1. pepper-pot mask design rules

The pepper-pot mask is a square array of holes of same diameter  $d$ , with the distance between their centers given by its pitch  $\Lambda$ . The material of the mask should be selected in a way that the particles propagating through it are absorbed or scattered at large angles. A high- $Z$  material, e.g., Tungsten, is commonly used in pepper-pot masks due to its high stopping power. The thickness  $t$  of the mask must be chosen such that it is larger than the radiation length of the material used,  $t \geq X_0$ . If Tungsten is used, the radiation length  $X_0$  of Tungsten is approximated as [36, 37],

$$X_0 = \frac{E}{\frac{dE}{dx}} \approx \frac{E \text{ (MeV)}}{1.5 \text{ (MeV cm}^2 \text{ g}^{-1}) \rho \text{ (gcm}^{-3})}, \quad (10)$$

where  $E$  is the energy of the incident beam, and  $\rho = 19.3 \text{ gcm}^{-3}$  is the density of the Tungsten material chosen for the mask.

Choosing the thickness of the mask is the first design rule of the pepper-pot method. The next design rule for the mask, regards the distance in which the screen should be placed downstream from the mask,  $L_{\text{drift}}$ . To avoid overlap between the beamlets in the screen, the distance  $L_{\text{drift}}$  should be chosen such that the condition  $4\theta_x L_{\text{drift}} < \Lambda$  is fulfilled [36]. Finally, the imaging system of the electron beam diagnostic should be capable of resolving the angular spread of the beamlets on the screen. Therefore, the position and angular resolution of the imaging system should be comparable,  $\sigma_x/\Lambda = L_{\text{drift}}\theta_x/r_i$ , where  $\sigma_x$  stands for the size of the beam and  $r_i$  is the resolution of the imaging system given in  $\mu\text{m}/\text{pixel}$ .

These conditions are easily fulfilled for RF-photoinjector beams, which typically have beam

waists around 0.5 mm and an rms divergence of the same order of magnitude, approximately 0.5 mrad. For instance, such beams can be adequately sampled by pepper-pot masks with hole diameters of 100  $\mu\text{m}$ , a pitch of about 200  $\mu\text{m}$ , and a screen placed approximately 60 cm from the mask [37].

In contrast, due to the significant difference of three orders of magnitude between waist size and divergence and also beam energy, LWFA beams hardly satisfy these design criteria. Consequently, the validity of using pepper-pot masks to measure LWFA/plasma-photocathode beams is at least questionable. In the following sections, we investigate the pepper-pot method with respect to LWFA parameters and find that the method is unable to accurately resolve the emittance of this class of electron beams.

### 2. Evaluating the beam emittance

After the interaction of beamlets with the screen, the emitted scintillation light is imaged, and the signal is integrated over the x- and y-axis. The integrated signal is then used to evaluate the rms emittance of the electron beam by applying the following equation which uses the second central moment of the particle distribution  $\langle x^2 \rangle$ ,  $\langle x'^2 \rangle$ , and  $\langle xx' \rangle$  previously introduced in Eq. (6) [2, 44],

$$\epsilon_{\text{rms}}^2 = \frac{1}{N^2} \left\{ \left[ \sum_{j=1}^p n_j (x_j - \bar{x})^2 \right] \times \left[ \sum_{j=1}^p \left[ n_j \sigma_{x_j}'^2 + n_j (x_j' - \bar{x}')^2 \right] \right] - \left[ \sum_{j=1}^p n_j x_j x_j' - N \bar{x} \bar{x}' \right]^2 \right\}, \quad (11)$$

where  $N = \sum_{j=1}^p n_j$ , and  $n_j$  is the number of electrons propagating within the  $j^{\text{th}}$  beamlet,  $x_j$  is the position of the  $j^{\text{th}}$  beamlet, and  $\bar{x}' = \sum_{j=1}^p n_j x_j' / N$  is the mean hole position. The rms divergence of the  $j^{\text{th}}$  beamlet is given by  $\sigma_{x_j}'$ ,  $x_j' = (X_j - x_j) / L_{\text{drift}}$  is the divergence of the  $j^{\text{th}}$  beamlet,  $X_j$  is the peak position of the beam passing through the  $j^{\text{th}}$  mask hole,  $\bar{x}'$  is the mean divergence of all beamlets, and  $p$  is the total number of beamlets.

The angular spread contribution exclusively from the emittance of the beam  $\sigma_{x_j}'^2$  must be deconvolved in quadrature from the beamlet distribution as [2, 37],

$$\sigma_{x_j}'^2 = \frac{\sigma_{\text{beamlet}_j}^2 - (dM/\sqrt{12})^2}{L_{\text{drift}}^2}, \quad (12)$$

where the term  $(dM/\sqrt{12})$  is the rms of the magnified beamlet diameter when considering it being a flat-top

distribution. The term  $\sigma_{\text{beamlet}_j}$  is given by the measurement of the rms size of each beamlet at the scintillation screen during the experiment. This value is obtained by fitting a Gaussian distribution on each of the beamlets on the image screen.

### III. TESTING THE PEPPER-POT METHOD

#### A. GEANT4 simulation setup

To evaluate how well the PP method works and identify its limitations (with an emphasis on parameters typical of LWFA beams), we conducted GEANT4 Monte-Carlo simulations [45–47] with parameters closely matching the experiment described later.

The distance between the source and PP mask is  $L_{\text{pp}} = 181$  mm and the distance between the mask and scintillation screen (detector position) is given by  $L_{\text{drift}} = 1269$  mm. The geometrical magnification of the experimental layout is  $M \approx 8$ . Different virtual screens (i.e. for numerical evaluation only) were placed in the simulation volume to record the parameters of the electrons propagating through them.

A total of  $3 \times 10^6$  primary electrons were generated at the source point, with parameters equivalent to those analyzed in the LWFA experiment discussed later. Consequently, the energy spectrum of the primary beam in the simulations was characterized by a Gaussian distribution, with a mean energy of 72 MeV and an rms value of  $\sigma_E = 50$  MeV, corresponding to an energy spread of approximately  $(\sigma_E/E) \approx 52\%$ . Additionally, the rms divergence of the electron beam was set to  $\theta_x = 1.85$  mrad. Both of these parameters remained fixed throughout all simulation runs presented here. The emittance of the beam was varied by varying the source size.

The pepper-pot method was tested numerically by inferring the emittance using the parameters obtained from recorded electrons (position, momenta, and energy) at the virtual screen positioned at the same position as the experimental detector screen position. The electrons that propagated through the scintillation screen were binned with a resolution of 18  $\mu\text{m}/\text{pixel}$ . The baseline visible in the integrated signals was removed to enhance the signal-to-noise ratio. The background was caused by large-angle scattered particles and X-rays produced via bremsstrahlung on the mask.

Finally, an algorithm for calculating the rms emittance using equation (11) was applied to the baseline-removed integrated signals. To summarize, the evaluation steps of the algorithm for the emittance retrieval are the following: (i) identification of peaks representing the centers of each beamlet signal; (ii) fitting of individual Gaussian distributions to each beamlet signal and storing their respective values of  $n_j$  and  $\sigma_{\text{beamlet}_j}$ ; (iii) calculation of the deconvolved beamlet angular spread  $\sigma'_{x'_j}$  using equation (12); (iv) evaluation of the rms emittance of the beams using equation (11).

The common approach of fitting a Gaussian [2] presumes that the size of each beamlet on the screen is dominated by its emittance, i.e., that the beamlet size is much larger than the point projection image of the PP hole. Note that if the PP signal at the screen is integrated vertically, i.e., in the y-direction, the emittance evaluated corresponds to the emittance in the x-direction. Similarly, integrating the beamlet signal in the x-direction results in the emittance in the y-direction.

#### B. Beam emittance for various source sizes

With the simulation volume and parameters established, multiple simulations were conducted for various source sizes, corresponding to different rms emittances. Additionally, masks with various hole diameters were employed to evaluate the performance of the pepper-pot method. The rms emittance of the primary electron beam in the simulations was altered solely by modifying the beam's source size. The beam's emittance was then inferred using the algorithm steps described above.

The results of the different simulation runs for two different pepper-pot geometries are shown in Fig. 1. In the left panel, a comparison between the input and inferred emittance from the simulations is presented for a pepper-pot mask with a pitch between holes of 120  $\mu\text{m}$ , and the center panel compares the emittance values for a pepper-pot mask with a pitch of 150  $\mu\text{m}$ . The GEANT4  $\epsilon_{\text{rms}}$  is calculated using Eq. (6) where the beam divergence and waist are from the test electron beam of each simulation run.

Curves of the form

$$\epsilon_{\text{rms}}^2 = \alpha^2 + \theta_x^2 \sigma_x^2, \quad (13)$$

were fitted to the data points obtained via the simulations shown in Fig. 1. Here,  $\theta_x$  in mrad and  $\sigma_x$  in  $\mu\text{m}$  stands for the divergence and source of the electron beam, respectively, and  $\alpha \approx 6.3 \mu\text{m mrad}$  is a constant value which will be examined in the next section.

From these simulation results, we can identify three regions in each plot given in Fig. 1. The first region observed is found at low emittance values  $< 10 \mu\text{m mrad}$  where the beam emittance is no longer resolved, resulting in an overestimation of the true value. The second region corresponds to values  $> 35 \mu\text{m mrad}$  where the emittance of the beam is underestimated, and the third area is found in between both previous limits where the source size is correctly estimated. Each of these regions is examined in detail in the next sections.

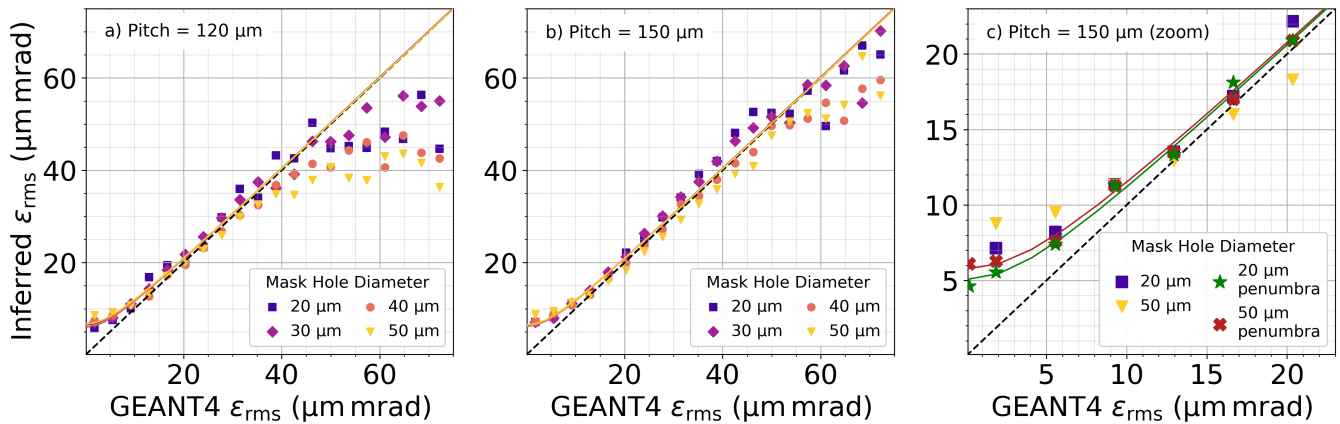


FIG. 1. Inferred emittance obtained via GEANT4 simulations for pepper-pot masks with two different hole pitches: (a) 120  $\mu\text{m}$  and (b) 150  $\mu\text{m}$ , along with various hole diameters. A detailed image with results using the penumbral deconvolution method for the pepper-pot with a pitch of 150  $\mu\text{m}$  at lower emittance values is shown in (c). The simulations utilized a pepper-pot with a thickness of 200  $\mu\text{m}$  and a square grid of  $33 \times 33$  holes. The pepper-pot mask was positioned 181 mm downstream from the electron source, and the screen for imaging the beamlets and inferring the emittance was placed 1269 mm downstream from the mask. The simulations were conducted with a primary electron beam consisting of  $3 \times 10^6$  particles, with an average mean energy of 72 MeV and a root-mean-square divergence of  $\theta_x = 1.85$  mrad. Curves of the form  $\epsilon_{\text{rms}}^2 = \alpha^2 + \theta_x^2 \sigma_x^2$  were fitted to the simulated data points. For more details on the values of the fitting parameters,  $\alpha$  and  $\theta_x$ , please see Appendix A. The black dashed line represents only the diagonal.

#### IV. LIMITATIONS OF THE PEPPER-POT METHOD

##### A. Problem resolving low emittance values

In the first region of interest, where the emittance is below 10  $\mu\text{m mrad}$ , the electron beam exhibits a small source size with a fixed divergence. Under these beam conditions, the angular spread of the beamlets is dominated by the point projection of the PP-holes. The finite source size is visible in the penumbral broadening of the individual beamlets on the screen. Consequently, the Gaussian distributions on each beamlet are a poor fit to the beamlet shape. The conventional data analysis method previously mentioned in section II B 2, then incorrectly assumes the angular spread  $\sigma_{\text{beamlet}}$  to be due to emittance only and returns a value comparable in magnitude to the term  $(dM/\sqrt{12})$  given in Eq. (12). Hence, the angular spread inferred by the Gaussian fit tends towards a constant (sometimes even a negative) value. With an increase in beam waist, the Gaussian fit returns a good estimate of the beamlet angular spread, as the spread due to emittance now exceeds the point projection contribution.

This issue is illustrated in Fig. 2, where various Gaussian fits on beamlets from different source sizes but with fixed divergence are shown. For small source sizes, i.e.,  $\sigma_{\text{rms}} < 10$   $\mu\text{m}$ , the Gaussian fit does not represent the data well, and the value of the deconvolved angular spread in this range is  $\approx 60$   $\mu\text{rad}$ .

In the absence of scattering, the shape of the beamlet is generally accurately described by a convolution  $i(x)$  between the source  $s(x)$  with the hole  $h(x)$  and is given

by [48, 49],

$$i(x) = h(x) * s(x). \quad (14)$$

A natural approach to obtaining the source's size is then to deconvolve the image with the hole function. In our case, the function  $i(x)$  is obtained by integrating the signals of the beamlets on the screen, and  $h(x)$  is a top-hat function representing the magnified hole of the mask.

One can deconvolve the function  $i(x)$  to obtain  $s(x)$  using, for example, Wiener filters [48]. We applied this method to the simulation results for emittances less than 20  $\mu\text{m mrad}$  from the pepper-pot mask with a 150  $\mu\text{m}$  pitch.

By deconvolving the penumbral image of the beamlet, the  $\sigma_x$  value of the source can, in principle, be directly obtained. The results of the analysis performed for source sizes of 0.1  $\mu\text{m}$  and 1.0  $\mu\text{m}$  are shown in Figs. 2 a) and b). From these results, we observe that the convolution provides a better fit than the typically used Gaussian fit. Consequently, the inferred source sizes  $\sigma_x$  for these small emittance beams are also reduced, as seen in Fig. 1 c).

For the simulation results analyzed using the penumbral deconvolution method shown in Fig. 1 c), the constant parameter  $\alpha$  given in Eq. (13) reduces from an average of 6.3  $\mu\text{m mrad}$  to smaller values:  $\alpha \approx 5.8$   $\mu\text{m mrad}$  for the pepper-pot with a hole diameter of 50  $\mu\text{m}$ , and  $\approx 5.1$   $\mu\text{m mrad}$  for the pepper-pot with a hole diameter of 20  $\mu\text{m}$ . Therefore, despite reducing the inferred emittance obtained by applying the deconvolution method to the penumbra of the beamlet projected onto the screen, the pepper-pot method still fails to resolve very small sizes. Ultimately, limitations in correctly inferring the

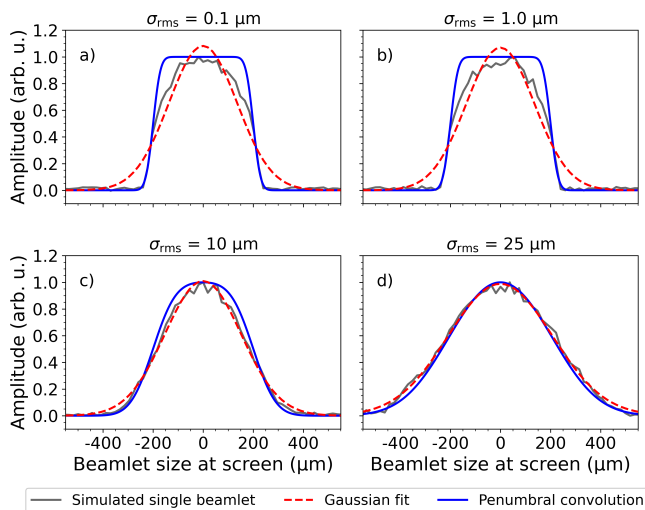


FIG. 2. Gaussian curve (red dashed line) and penumbral convolution (blue solid line) between a Gaussian source and the mask holes fitted to the simulated beamlet image (solid gray line) for various beam waists  $\sigma_{\text{rms}}$  while maintaining a fixed beam divergence of 1.85 mrad. For small source sizes, i.e., small beam emittances, the Gaussian fit is ill-posed, and the beamlet projection on the screen is best represented by the convolution between the mask hole function and the Gaussian distribution of the source as seen in Eq. (14). However, as the source beam waist  $\sigma_x$  increases, the Gaussian fit can more accurately represent the signal, as the contribution of the beamlet becomes smaller compared to the mask hole projection. The simulated beamlet response on the screen was generated using the GEANT4 Monte Carlo framework.

small effects on the overall beamlet size due to the source size prove to be the practical limit.

To mitigate the limitations of the pepper-pot method in resolving small emittances, several options can be considered. For example, one could reduce the pitch distance or the diameter of the mask holes. However, by reducing the diameter of the holes, the number of particles propagating through them is reduced, making it challenging to achieve a signal-to-noise ratio at the screen much larger than one. In addition, this presents challenges with the current technology available for machining tiny holes in pepper-pot masks. The conventional method involves laser drilling, which is limited by the thickness of the mask in terms of the hole diameters it can produce. If smaller holes are required, the thickness of the mask must also be reduced. However, reducing the mask thickness results in fewer electrons being scattered at larger angles or being stopped, leading to a larger Gaussian background noise that can reduce the accuracy of the emittance measurement.

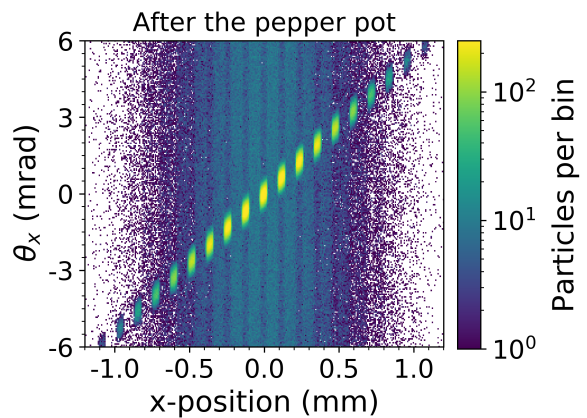


FIG. 3. Simulated trace space of an electron beam with a 40  $\mu\text{m}$  source size after its interaction with a pepper-pot mask with a hole diameter of 50  $\mu\text{m}$  and a pitch of 120  $\mu\text{m}$ . The trace space of the beam is sampled in beamlets, and background noise arises due to electrons that are scattered at large angles. The simulation was performed with the GEANT4 Monte Carlo framework, with a distance of 181 mm between the primary electron source and the pepper-pot mask. The beam emittance for this simulation is 74  $\mu\text{m mrad}$ , which represents the last point of the result shown in Fig. 1 a) for the 50  $\mu\text{m}$  hole diameter mask.

### B. Underestimating large emittance values

For values above  $> 35 \mu\text{m mrad}$ , the emittance values are underestimated for large source sizes, as observed in the plots of Fig. 1. The reason why the method fails to infer correctly the emittance values in this region is better understood by examining the trace space of the beam after its interaction with the mask and at the detection plane, as shown in Fig. 3.

The sampling of the beam into beamlets in the pepper-pot mask is represented by the trace space shown in Fig. 3. As the beamlets propagate from the mask to the detection screen, the trace space of each individual beamlet rotates, and the beamlets rapidly spread due to their angular divergence. As the overlap intensifies, the baseline of the integrated signal (in the angular direction) also elevates, since the beamlets now start to overlap each other, diminishing the signal-to-noise ratio of the individual beamlets during post-processing of the data. The beamlet overlap can be minimized during data evaluation through the implementation of baseline correction. However, applying baseline reduction during data analysis also reduces the height  $n_j$  and rms spread  $\sigma_{\text{beamlet}_j}$  of the beamlets, resulting in an underestimation of the inferred emittance when using Eq. (11).

To effectively mitigate these overlapping effects, a larger distance between the pepper-pot holes (pitch) can be utilized. A comparison between the integrated signal obtained from different masks with pitches of 120  $\mu\text{m}$  and 150  $\mu\text{m}$  is shown in Fig. 4. For the simulations employing a large pitch distance in the pepper-pot, the beam-

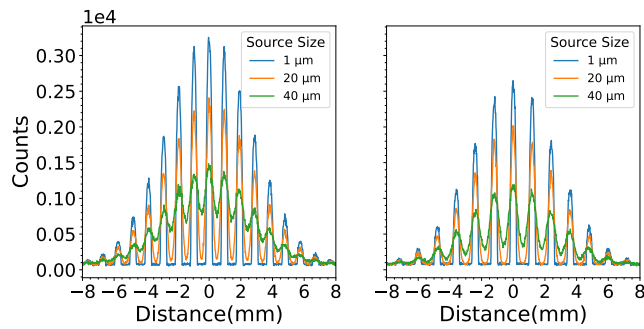


FIG. 4. (Left) Integrated signals (summation over the y-axis to investigate  $\epsilon_x$ ) from GEANT4 simulation results of the beamlet signal at the screen for a pepper-pot mask with a hole diameter of 50  $\mu\text{m}$  and a pitch distance of 120  $\mu\text{m}$ . The elevated signal due to beamlet overlap is significant for the larger source-size beam. (Right) Integrated signal for a pepper-pot mask with the same hole diameter of 50  $\mu\text{m}$  but a larger pitch of 150  $\mu\text{m}$ . The overlap between the beamlets is reduced, resulting in a higher signal-to-noise ratio for individual beamlets during post-processing of the data.

lets for large source sizes have a reduced overlap (see the right panel of Fig. 4), contrasting with the integrated signals of the smaller pitch pepper-pot mask shown in the left panel of the same figure. This improvement is also noticeable in the results depicted in panels b) and c) of Fig. 1. Increasing the pitch distance of the pepper-pot mask reveals that the region where overlap occurs is situated at higher emittance values, in our case above 35 mm mrad. Consequently, the method becomes capable of characterizing a broader range of beam emittances. This adjustment in the pepper-pot mask design enables the method to diagnose beams with large emittances and source sizes.

To determine the minimum pitch distance to avoid overlap on the screen at the  $1/e^2$  level of the angular spread of the beamlets, a modified version of the condition given in Ref. [50] can be used:

$$\Lambda > \sqrt{2} \left[ 2\sigma_{\text{rms}} \left( 1 - \frac{L_{\text{pp}}}{L_{\text{drift}}} \right) + d \right], \quad (15)$$

where  $d$  is the hole diameter of the mask, and  $\sigma_{\text{rms}}$  is the source size of the electron beam. The condition given in Eq.(15) depends on the distance between the electron beam source and the mask,  $L_{\text{pp}}$ , and the screen distance from the pepper-pot,  $L_{\text{drift}}$ . For larger distances,  $L_{\text{drift}}$ , the pitch between the mask holes should also be increased. The  $\sqrt{2}$  term arises from the conversion of a top-hat function to the beam waist of a Gaussian.

To verify this condition, it can be applied to the simulation data shown in Fig.1. For example, for an input GEANT4 rms emittance of 40  $\mu\text{m}$  mrad and a mask with holes of diameter  $d = 50 \mu\text{m}$ , the minimum pitch required for imaging the beamlets on the screen (for the simulated setup) is  $\Lambda \gtrsim 123 \mu\text{m}$ . By analyzing the simulation results, we observe that with a pitch of 120  $\mu\text{m}$ ,

the mask with 50  $\mu\text{m}$  holes starts to fail in resolving emittances around 40  $\mu\text{m}$  mrad as predicted by Eq. (15), corresponding to a source size of  $\approx 21.6 \mu\text{m}$ . On the other hand, when the pitch is increased to 150  $\mu\text{m}$ , the pepper-pot with the same hole diameter successfully resolves the emittance of the electron beam with the same source size.

### C. Pepper-pot operating regime

For values in the range between 10 to 35  $\mu\text{m}$  mrad, the pepper-pot method accurately resolves the beam emittance for our conditions. In contrast to the limiting regions described previously, here the overlap between the beamlets is minimal, enabling the correct retrieval of their individual spreads and heights after the removal of background noise (baseline).

For these intermediate source sizes  $> 10 \mu\text{m}$  for our parameters, the Gaussian fit provides an equally good or even slightly better fit to the calculated signal, as seen in Figs. 2 c) and d) allowing the emittance to be inferred using the method described in section II B 2.

The PP operating regime is identified by the angular spread of the beamlets and the source sizes being significant enough that the second term on the right-hand side of equation (13) predominates over the constant term  $\alpha$ . Consequently, the dependence on the experimental layout of the setup is minimized, and the emittance is approximated by the beam parameters as  $\epsilon_{\text{rms}} \approx \theta_x \sigma_x$ .

## V. THE PEPPER-POT EXPERIMENT

In this section, we describe an experiment performed at the JETi200 laser system at the Helmholtz Institute Jena (Germany) performed to measure the emittance of LWFA electron beams using the pepper-pot method.

The experiment layout was closely matched by the geometry in the Monte Carlo simulations discussed previously.

### A. Experimental setup

The experiment was set up at the JETi200 laser system at the Helmholtz Institute Jena (Germany). The laser system provides laser pulses with an energy of 4.6 J centered at 800 nm, and a pulse duration of 23 fs. The experimental setup is illustrated in Fig. 5.

In the experiment, the beam was reduced from its original size of 120 mm to a smaller diameter of 60 mm by a splitting mirror resulting in a total beam energy of 1.15 J. The laser beam was focused by an off-axis parabolic mirror (f-number = 16.7) to a spot with  $(23.7 \pm 1.8) \mu\text{m}$  at full width at half maximum (FWHM) with approximately 38% of the pulse energy within the FWHM, resulting in a peak intensity of  $7 \times 10^{18} \text{ W cm}^{-2}$ . The focused laser beam impinged on a supersonic gas jet (mixture of 95%

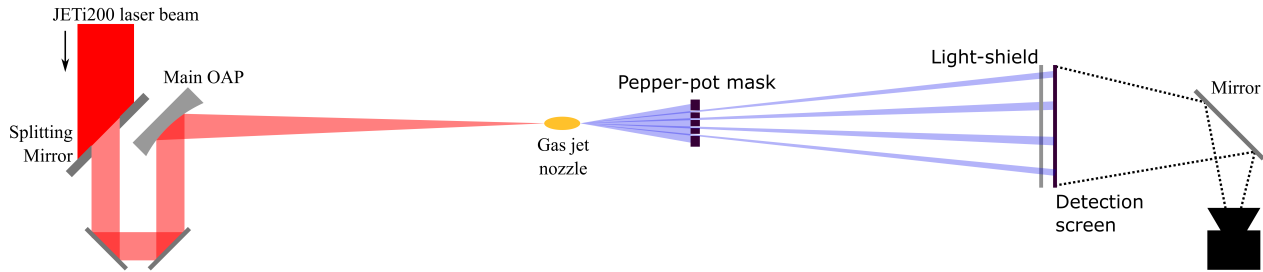


FIG. 5. Experimental layout for emittance measurements using the pepper-pot mask. The pepper-pot mask is placed on the beam axis for the formation of the beamlets that are imaged utilizing a scintillation screen.

He and 5% N<sub>2</sub>) generating an underdense plasma with an electron density of  $1.1 \times 10^{19} \text{ cm}^{-3}$  in the plateau region to be injected in the plasma bubble mainly via ionization injection [51].

In the experiment, the distance between the exit of the gas jet nozzle and the PP was about  $L_{pp} = (180 \pm 1) \text{ mm}$ . Finally, the distance from the PP to the YAG:Ce scintillating screen was approximately  $L_{drift} \approx (1269 \pm 1) \text{ mm}$ . The geometrical magnification of the setup was  $M = (L_{pp} + L_{drift})/L_{pp} \approx 8$ .

The pepper-pot used in this experiment has a square grid of  $33 \times 33$  holes of  $d \approx 50 \text{ }\mu\text{m}$  diameter with a pitch length of  $\approx 120 \text{ }\mu\text{m}$ . The mask is  $200 \text{ }\mu\text{m}$  thick and made of tungsten (density of  $19.3 \text{ g/cm}^3$  and collision stopping power of about  $1.4 \text{ MeV cm}^2 \text{ g}^{-1}$  for 73 MeV electrons [52]) which is enough to scatter few MeV electrons into large angles.

As the beam propagates through the mask, the remaining beamlets travel towards a YAG:Ce scintillation screen (detection plane) of  $100 \text{ }\mu\text{m}$  thickness primarily emitting at approximately 550 nm wavelength and imaged by an Andor Marana camera (16-bit, quantum efficiency  $\approx 95\%$  at 550 nm) [53] with optical resolution of the imaging system at the scintillator screen calibrated to be  $r_i \approx 18.5 \text{ }\mu\text{m}/\text{pixel}$ . To avoid background noise in the electron signal in the screen caused by the scattered laser light, an Al-foil of  $\approx 100 \text{ }\mu\text{m}$  thickness was placed about 10 mm in front of the screen to light shield the diagnostic.

## B. Electron beam characteristics

The LWFA electron beam had a maximum energy of about 120 MeV with a total charge of approximately  $(5.6 \pm 0.7) \text{ pC}$ . The electron energy distribution has a weighted average of approximately 73 MeV, equivalent to  $\langle \gamma \rangle \approx 143$ , and a weighted average energy spread of  $(\sigma_E/E) = (27.3 \pm 4.8)\%$ .

The rms divergence of the beam in the x-direction obtained during the experiment was evaluated to be  $\theta_x \approx (1.8 \pm 0.3) \text{ mrad}$ . To determine its value, we removed the pepper-pot mask from the beam path and

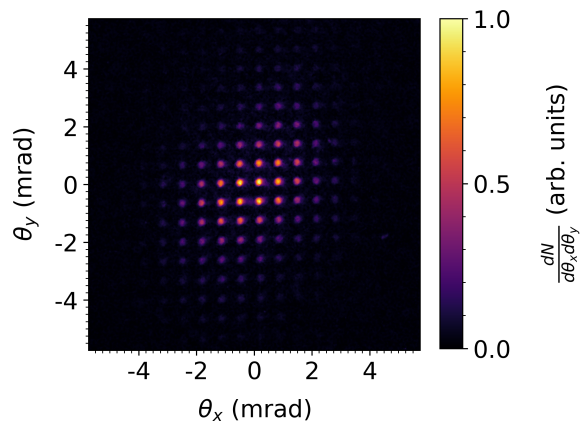


FIG. 6. Example of beamlets imaged using a scintillation screen. The pepper-pot mask had a  $50 \text{ }\mu\text{m}$  hole size. An average distance between beamlets of  $(953.6 \pm 15.2) \text{ }\mu\text{m}$  at the screen was measured.  $\theta_x, \theta_y$  represent the beam divergence coordinates.

recorded the beam profile on the detection screen. For each captured beam profile, a two-dimensional Gaussian was fitted to obtain their respective rms spread. Finally, the beam divergence was calculated by averaging all evaluated spreads, with the error determined by their standard deviation.

For more information on the electron beam, please see the details in our previous publication found in Ref. [31] which utilizes a similar setup for the laser-accelerated electron beams.

## C. Emittance measurement using pepper-pot mask

Figure 6 shows an example of pepper-pot beamlets imaged on the YAG:Ce screen. To calculate the emittance using Eq. (11), we used the same post-processing steps and algorithm described previously in section III.

After analyzing 100 shots we obtained an average geometrical emittance of  $\epsilon_{rms,exp} = (26.2 \pm 7.3) \times 10^{-3} \pi \text{ mm mrad}$  for the pepper-pot mask with  $50 \text{ }\mu\text{m}$



hole size and 120  $\mu\text{m}$  pitch, where the uncertainty is given by the standard deviation of all analyzed shots.

This result was compared to the GEANT4 simulation results as shown in Fig. 7. The inferred experimental value matches the predicted values for source sizes below the pepper-pot resolution limit. From the figure, one can see, that our PP implementation can only resolve emittances within a 10% error in a small range between 35 to 40  $\mu\text{m mrad}$ , which is highlighted as the shaded gray area in Fig. 7.

Solving equation (13) for the beam waist  $\sigma_{x_{\text{exp}}}$ , an average beam waist of our test electron beams yields  $\sigma_{x_{\text{exp}}} \approx 9.7 \mu\text{m}$ . This value given by the PP method is much larger than the upper limit of 1.7  $\mu\text{m}$  previously reported using the laser grating method to evaluate the source size of similar electron beams [31]. Our pepper-pot data agrees with previous results, for example, in Ref. [2], where the beam waist for a LWFA beam was evaluated to be approximately 21  $\mu\text{m}$ , in agreement with the limits for the technique predicted by our simulations.

For emittance values above 40  $\mu\text{m mrad}$ , the method cannot resolve the beam's emittance, underestimating the real value. In this region, the beamlets overlap as explained in the previous section IV B, and when applying baseline reduction on the integrated data, there is a reduction in the height  $n_j$  of the beamlets and, consequently, the rms spread  $\sigma_{\text{beamlet}_j}$ . To fix this error, one could employ a PP mask with a larger pitch between holes to avoid the overlap of the beamlet signals in the detection screen.

In our setup, the large error in accurately inferring the rms emittance occurs due to the addition of the Al-foil used for light-shielding, which leads to an artificial emittance growth in the low-emittance range of less than 15  $\mu\text{m mrad}$ , since the Al-foil scatters few-MeV particles, increasing the background noise on the detection screen.

For completeness, the averaged normalized emittance was evaluated using Eq. (9) for the experimental data results in  $\epsilon_n \approx 158.8 \pi \text{ mm mrad}$ . The large normalized emittance value arises due to the large energy spread of the electron beam, resulting in different phase space rotation speeds of the particles while freely drifting toward the screen. This large value can also be understood by examining Eq. (9). Due to the substantial energy spread and drift length, the first term on the right-hand side is much larger than the rms emittance term,  $(\sigma_E/E)^2 \theta_x^4 L_{\text{drift}}^2 \gg \epsilon_{\text{rms}}^2$ . Consequently, the normalized emittance is dominated by the growth of the transverse distribution of the beam.

Our normalized emittance is found to be larger than the values reported in the literature for LWFA beams, such as in Refs. [1–3, 32, 33]. The discrepancy arises because we calculate the normalized emittance taking into account the broadband energy spectrum of our electron beam, a consideration that is not accounted for in the cited literature, which considers their energy spread to be negligible as found in conventional RF-accelerators.

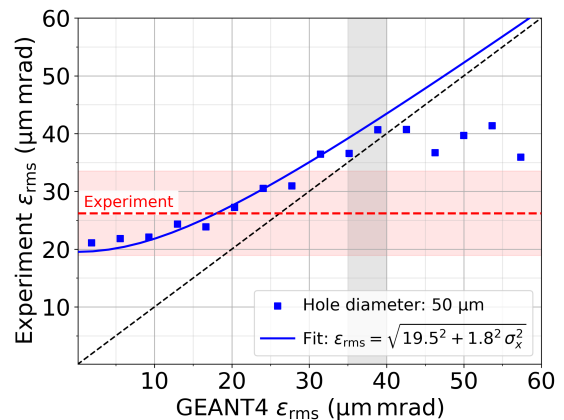


FIG. 7. Comparison of the experimental data with the simulated data for our setup. We infer a value of  $(26.2 \pm 7.3) \mu\text{m mrad}$ . This matches the lower limit of the simulated response for our pepper-pot geometry, implying that the real source size cannot be experimentally resolved by the pepper-pot. The shaded area in red around the experimental result indicates the uncertainty span of the inferred value. The solid blue curve represents a fit on the inferred emittances obtained via GEANT4 Monte-Carlo simulations. The fit equation is:  $\epsilon_{\text{rms}} = \sqrt{19.5^2 + 1.8^2 \sigma_x^2}$  and was performed for the points below 40  $\mu\text{m mrad}$ .

## VI. CONCLUSIONS

The pepper-pot method is widely used to measure beam emittance, but it has limitations that affect its accuracy, especially in resolving very low emittance values. Such low emittance beams are commonly found in linacs and LWFA accelerators. In the low emittance regime, below 10  $\mu\text{m mrad}$ , the method struggles due to the dominance of the point projection image over the actual angular spread of the beamlets. This leads to poor emittance estimates based on fitted Gaussian distributions. One can attempt to extend the accuracy of the PP technique for small source sizes using penumbral deconvolution techniques. While this improves the accuracy of the inferred source sizes for small emittance beams, it still does not allow for accurate resolution of the emittance due to the small effects of the source size on the overall beamlet size.

For large emittance values, above 35  $\mu\text{m mrad}$  for our parameters, the method underestimates the emittance due to significant beamlet overlap and the resulting elevated baseline of the integrated signal. Adjustments such as increasing the pitch distance between the holes in the pepper-pot mask help to mitigate these effects, enabling the method to better characterize beams with large emittance.

In the intermediate range (from 10 to 35  $\mu\text{m mrad}$  for our parameters), the pepper-pot method accurately resolves the beam emittance. Here, the beamlets' angular spread and source sizes are sufficiently large, reducing the influence of the experimental setup's geometric param-

ters and allowing reliable emittance measurements.

To demonstrate the limitations of the pepper-pot method in resolving the emittance of laser-accelerated electron beams, we performed an experiment at the JETi200 laser system and compared the obtained source size with the more accurate laser grating technique. Using the pepper-pot a source size of approximately  $9.7 \mu\text{m}$  and an rms emittance of  $(26.2 \pm 7.3) \times 10^{-3} \pi \text{ mm mrad}$  was obtained. The inferred source size is substantially larger than the upper limit determined using the laser grating method under the same experimental conditions as reported in our previous work ( $1.7 \mu\text{m}$  [31]).

For typical LWFA experiments with source sizes in the few micron range, the pepper-pot technique cannot provide accurate measurements for small emittances. The technique is more suited for large emittances, where increasing the hole diameter and pitch distance in the pepper-pot geometry allows for better resolution. However, other techniques such as quadrupole scans and, for the smallest emittances of the order of nanometers [54], the laser-grating method may be more appropriate [30, 31]. Each pepper-pot configuration has a limited range of emittance values it can measure accurately, meaning that different geometries are required depending on the actual emittance value.

## VII. ACKNOWLEDGEMENTS

The authors thank G. Schäfer for operating the JETi200- laser system. This research was funded by the Federal Ministry of Education and Research of Germany (BMBF) in the Verbundforschungsframework (Project Nos. 05K19SJA, 05K22SJB and 05K22SJA). F.C.S. and M.Z. thank the funding by the Deutsche Forschungsgemeinschaft (DFG) under Project No. 416708866 within the Research Unit FOR2783. The research leading to the presented results received additional funding from the European Regional Development Fund and the State of Thuringia via Thüringer Aufbaubank TAB (Contract Nos. 2019 FGI 0013, 2022 FGI 0003, 2022 FGI 0005 and 2023 FGI 0023).

## Appendix A: Fitting parameters for the Monte-Carlo simulations

In Fig. 1, curves of the form  $\epsilon_{\text{rms}}^2 = \alpha^2 + \theta_x^2 \sigma_x^2$  were fitted to the data points from the Monte Carlo simulations performed for various pepper-pot masks with two different hole pitch distances.

The fitting parameters,  $\alpha$  and  $\theta_x$ , for the curve fitted to the simulated results of the PP mask with a pitch distance of  $120 \mu\text{m}$ , as shown in Fig. 1a), are given in Table I.

For the curves fitted to the data points of the PP mask with a  $150 \mu\text{m}$  pitch in Figs. 1 b) and c), the fitting parameters are given in Table II. The table also includes

Table I. Fitting parameters for the curves presented in Fig. 1 a) where the PP mask has a hole pitch of  $120 \mu\text{m}$ .

PP hole diameter ( $\mu\text{m}$ )	$\alpha$ ( $\mu\text{m mrad}$ )	$\theta_x$ (mrad)
20	0.60	1.85
30	0.43	1.85
40	0.30	1.84
50	0.27	1.84

the fitting parameters for the emittance inferred using the penumbral deconvolution method.

Table II. Fitting parameters for the curves presented in Fig. 1 b) and c) where the PP mask has a hole pitch of  $150 \mu\text{m}$ .

PP hole diameter ( $\mu\text{m}$ )	$\alpha$ ( $\mu\text{m mrad}$ )	$\theta_x$ (mrad)
20	0.64	1.85
30	0.42	1.85
40	0.31	1.84
50	0.26	1.84
20 (penumbra)	0.51	1.85
50 (penumbra)	0.23	1.85

Note that, in all fitting results, the beam divergence  $\theta_x \approx 1.85 \text{ mrad}$  which is the constant beam divergence used in the simulations.

- [1] R. P. Shanks, M. P. Anania, E. Brunetti, S. Cipiccia, B. Ersfeld, J. G. Gallacher, R. C. Issac, M. R. Islam, G. Vieux, G. H. Welsh, S. M. Wiggins, and D. A. Jaroszynski, Pepper-pot emittance measurement of laser-plasma wakefield accelerated electrons, in *Harnessing Relativistic Plasma Waves as Novel Radiation Sources from Terahertz to X-Rays and Beyond*, SPIE Proceedings, edited by D. A. Jaroszynski and A. Rousse (SPIE, 2009) p. 735907.
- [2] C. M. S. Sears, A. Buck, K. Schmid, J. Mikhailova, F. Krausz, and L. Veisz, Emittance and divergence of

laser wakefield accelerated electrons, *Phys. Rev. ST Accel. Beams* **13**, 092803 (2010).

- [3] G. G. Manahan, E. Brunetti, C. Aniculaesei, M. P. Anania, S. Cipiccia, M. R. Islam, D. W. Grant, A. Subiel, R. P. Shanks, R. C. Issac, G. H. Welsh, S. M. Wiggins, and D. A. Jaroszynski, Characterization of laser-driven single and double electron bunches with a permanent magnet quadrupole triplet and pepper-pot mask, *New J. Phys.* **16**, 103006 (2014).
- [4] W. Wang, K. Feng, L. Ke, C. Yu, Y. Xu, R. Qi, Y. Chen, Z. Qin, Z. Zhang, M. Fang, J. Liu, K. Jiang, H. Wang,

- C. Wang, X. Yang, F. Wu, Y. Leng, J. Liu, R. Li, and Z. Xu, Free-electron lasing at 27 nanometres based on a laser wakefield accelerator, *Nature* **595**, 516 (2021).
- [5] M. Fuchs, R. Weingartner, A. Popp, Z. Major, S. Becker, J. Osterhoff, I. Cortie, B. Zeitler, R. Hörlein, G. D. Tsakiris, U. Schramm, T. P. Rowlands-Rees, S. M. Hooker, D. Habs, F. Krausz, S. Karsch, and F. Grüner, Laser-driven soft-X-ray undulator source, *Nat. Phys.* **5**, 826 (2009).
- [6] Z. Huang, Y. Ding, and C. B. Schroeder, Compact x-ray free-electron laser from a laser-plasma accelerator using a transverse-gradient undulator, *Phys. Rev. Lett.* **109**, 204801 (2012).
- [7] A. R. Maier, A. Meseck, S. Reiche, C. B. Schroeder, T. Seggebrock, and F. Grüner, Demonstration Scheme for a Laser-Plasma-Driven Free-Electron Laser, *Phys. Rev. X* **2**, 031019 (2012).
- [8] W. Leemans and E. Esarey, Laser-driven plasma-wave electron accelerators, *Phys. Today* **62**, 44 (2009).
- [9] C. B. Schroeder, E. Esarey, C. G. R. Geddes, C. Benedetti, and W. P. Leemans, Physics considerations for laser-plasma linear colliders, *Phys. Rev. Spec. Top. Accel Beams* **13**, 101301 (2010).
- [10] ALEGRO collaboration, *Towards an Advanced Linear International Collider* (2019), 83 pages.
- [11] R. W. Assmann, M. K. Weikum, T. Akhter, D. Alesini, A. S. Alexandrova, M. P. Anania, N. E. Andreev, I. Andriyash, M. Artioli, A. Aschikhin, T. Audet, A. Bacci, I. F. Barna, S. Bartocci, A. Bayramian, A. Beaton, A. Beck, M. Bellaveglia, A. Beluze, A. Bernhard, A. Bigioni, S. Bielawski, F. G. Bisesto, A. Bonatto, L. Boulton, F. Brandi, R. Brinkmann, F. Briquez, F. Brottier, E. Bründermann, M. Büscher, B. Buonomo, M. H. Bussmann, G. Bussolino, P. Campana, S. Cantarella, K. Casou, A. Chancé, M. Chen, E. Chiadroni, A. Cianchi, F. Cioeta, J. A. Clarke, J. M. Cole, G. Costa, M.-E. Couprie, J. Cowley, M. Croia, B. Cros, P. A. Crump, R. D’Arcy, G. Dattoli, A. Del Dotto, N. Delerue, M. Del Franco, P. Delinikolas, S. de Nicola, J. M. Dias, D. Di Giovenale, M. Diomedede, E. Di Pasquale, G. Di Pirro, G. Di Raddo, U. Dorda, A. C. Erlandson, K. Ertel, A. Esposito, F. Falcoz, A. Falone, R. Fedele, A. Ferran Pousa, M. Ferrario, F. Filippi, J. Fils, G. Fiore, R. Fiorito, R. A. Fonseca, G. Franzini, M. Galimberti, A. Gallo, T. C. Galvin, A. Ghaith, A. Ghigo, D. Giove, A. Giribono, L. A. Gizzi, F. J. Grüner, A. F. Habib, C. Haefner, T. Heinemann, A. Helm, B. Hidding, B. J. Holzer, S. M. Hooker, T. Hosokai, M. Hübner, M. Ibson, S. Incremona, A. Irman, F. Iungo, F. J. Jafarinia, O. Jakobsson, D. A. Jaroszynski, S. Jaster-Merz, C. Joshi, M. Kaluza, M. Kando, O. S. Karger, S. Karsch, E. Khazanov, D. Khikhlikha, M. Kirchen, G. Kirwan, C. Kitégi, A. Knetsch, D. Kocon, P. Koester, O. S. Kononenko, G. Korn, I. Kostyukov, K. O. Kruchinin, L. Labate, C. Le Blanc, C. Lechner, P. Lee, W. Leemans, A. Lehrach, X. Li, Y. Li, V. Libov, A. Lifschitz, C. A. Lindström, V. Litvinenko, W. Lu, O. Lundh, A. R. Maier, V. Malka, G. G. Manahan, S. P. D. Mangles, A. Marcelli, B. Marchetti, O. Marcouillé, A. Marocchino, F. Marteau, A. La Martinez de Ossa, J. L. Martins, P. D. Mason, F. Massimo, F. Mathieu, G. Maynard, Z. Mazzotta, S. Mironov, A. Y. Molodozhentsev, S. Morante, A. Mosnier, A. Mostacci, A.-S. Müller, C. D. Murphy, Z. Najmudin, P. A. P. Nghiem, F. Nguyen, P. Niknejadi, A. Nutter, J. Osterhoff, D. Oumbarek Espinos, J.-L. Paillard, D. N. Papadopoulos, B. Patrizi, R. Pattathil, L. Pellegrino, A. Petralia, V. Petrillo, L. Piersanti, M. A. Pocsai, K. Poder, R. Pompili, L. Pribyl, D. Pugacheva, B. A. Reagan, J. Resta-Lopez, R. Ricci, S. Romeo, M. Rossetti Conti, A. R. Rossi, R. Rossmanith, U. Rotundo, E. Roussel, L. Sabbatini, P. Santangelo, G. Sarri, L. Schaper, P. Scherkl, U. Schramm, C. B. Schroeder, J. Scifo, L. Serafini, G. Sharma, Z. M. Sheng, V. Shpakov, C. W. Siders, L. O. Silva, T. Silva, C. Simon, C. Simon-Boisson, U. Sinha, E. Sistrunk, A. Specka, T. M. Spinka, A. Stecchi, A. Stella, F. Stellato, M. J. V. Streeter, A. Sutherland, E. N. Svystun, D. Symes, C. Szwej, G. E. Tauscher, D. Terzani, G. Toci, P. Tomassini, R. Torres, D. Ullmann, C. Vaccarezza, M. Valléau, M. Vannini, A. Vannozzi, S. Vescovi, J. M. Vieira, F. Villa, C.-G. Wahlström, R. Walczak, P. A. Walker, K. Wang, A. Welsch, C. P. Welsch, S. M. Weng, S. M. Wiggins, J. Wolfenden, G. Xia, M. Yabashi, H. Zhang, Y. Zhao, J. Zhu, and A. Zigler, EuPRAXIA Conceptual Design Report, *Eur. Phys. J. Spec. Top.* **229**, 3675 (2020).
- [12] C. G. Geddes, S. Rykovanov, N. H. Matlis, S. Steinke, J.-L. Vay, E. H. Esarey, B. Ludewigt, K. Nakamura, B. J. Quiter, C. B. Schroeder, C. Toth, and W. P. Leemans, Compact quasi-monoenergetic photon sources from laser-plasma accelerators for nuclear detection and characterization, *Nucl. Instrum. Methods Phys. Res., Sect. B* **350**, 116 (2015).
- [13] N. D. Powers, I. Ghebregziabher, G. Golovin, C. Liu, S. Chen, S. Banerjee, J. Zhang, and D. P. Umstadter, Quasi-monoenergetic and tunable X-rays from a laser-driven Compton light source, *Nat. Photonics* **8**, 28 (2014).
- [14] E. Esarey, C. B. Schroeder, and W. P. Leemans, Physics of laser-driven plasma-based electron accelerators, *Rev. Mod. Phys.* **81**, 1229 (2009).
- [15] M. Reiser, *Theory and design of charged particle beams*, 2nd ed. (Wiley-VCH, 2008).
- [16] G. G. Manahan, A. F. Habib, P. Scherkl, P. Delinikolas, A. Beaton, A. Knetsch, O. Karger, G. Wittig, T. Heinemann, Z. M. Sheng, J. R. Cary, D. L. Bruhwiler, J. B. Rosenzweig, and B. Hidding, Single-stage plasma-based correlated energy spread compensation for ultrahigh 6D brightness electron beams, *Nat. Commun.* **8**, 15705 (2017).
- [17] Z. Xiang, C. Yu, Z. Qin, X. Jiao, J. Cheng, Q. Zhou, G. Axi, J. Jie, Y. Huang, J. Cai, and J. Liu, Ultrahigh-brightness 50 MeV electron beam generation from laser wakefield acceleration in a weakly nonlinear regime, *Matter Radiat. Extremes* **9**, 035201 (2024).
- [18] R. Weingartner, S. Raith, A. Popp, S. Chou, J. Wenz, K. Khrennikov, M. Heigoldt, A. R. Maier, N. Kajumba, M. Fuchs, B. Zeitler, F. Krausz, S. Karsch, and F. Grüner, Ultralow emittance electron beams from a laser-wakefield accelerator, *Phys. Rev. Spec. Top. Accel Beams* **15**, 111302 (2012).
- [19] E. Prat and M. Aiba, Four-dimensional transverse beam matrix measurement using the multiple-quadrupole scan technique, *Phys. Rev. Spec. Top. Accel Beams* **17**, 052801 (2014).
- [20] F. Ji, J. G. Navarro, P. Musumeci, D. B. Durham, A. M. Minor, and D. Filippetto, Knife-edge based measurement of the 4D transverse phase space of electron beams with picometer-scale emittance, *Phys. Rev. Accel. Beams* **22**,

- 082801 (2019).
- [21] R. Akre, L. Bentson, P. Emma, and P. Krejcik, A transverse rf deflecting structure for bunch length and phase space diagnostics, in *PACs2001. Proceedings of the 2001 Particle Accelerator Conference (Cat. No.01CH37268)* (IEEE, 2001) pp. 2353–2355.
- [22] C. Behrens, F.-J. Decker, Y. Ding, V. A. Dolgashev, J. Frisch, Z. Huang, P. Krejcik, H. Loos, A. Lutman, T. J. Maxwell, J. Turner, J. Wang, M.-H. Wang, J. Welch, and J. Wu, Few-femtosecond time-resolved measurements of X-ray free-electron lasers, *Nat. Commun.* **5**, 3762 (2014).
- [23] V. A. Dolgashev, G. Bowden, Y. Ding, P. Emma, P. Krejcik, J. Lewandowski, C. Limborg, M. Litos, J. Wang, and D. Xiang, Design and application of multimegawatt X-band deflectors for femtosecond electron beam diagnostics, *Phys. Rev. Spec. Top. Accel Beams* **17**, 102801 (2014).
- [24] K. Floettmann and V. V. Paramonov, Beam dynamics in transverse deflecting rf structures, *Phys. Rev. Spec. Top. Accel Beams* **17**, 024001 (2014).
- [25] J. Maxson, D. Cesar, G. Calmasini, A. Ody, P. Musumeci, and D. Alesini, Direct Measurement of Sub-10 fs Relativistic Electron Beams with Ultralow Emittance, *Phys. Rev. Lett.* **118**, 154802 (2017).
- [26] J. Tan, W. Fang, D. Tong, Q. Gu, X. Huang, Z. Li, T. Higo, S. Matsumoto, T. Takatomi, and Z. Zhao, Design, RF measurement, tuning, and high-power test of an X-band deflector for Soft X-ray Free Electron Lasers (SXFEL) at SINAP, *Nucl. Instrum. Methods Phys. Res., Sect. A* **930**, 210 (2019).
- [27] B. Marchetti, A. Grudiev, P. Craievich, R. Assmann, H.-H. Braun, N. Catalan Lasheras, F. Christie, R. D’Arcy, R. Fortunati, R. Ganter, P. González Caminal, M. Hoffmann, M. Huening, S. M. Jaster-Merz, R. Jonas, F. Marcellini, D. Marx, G. McMonagle, J. Osterhoff, M. Pedrozzi, E. Prat Costa, S. Reiche, M. Reukauff, S. Schreiber, G. Tews, M. Vogt, S. Wesch, and W. Wünsch, Experimental demonstration of novel beam characterization using a polarizable X-band transverse deflection structure, *Sci. Rep.* **11**, 3560 (2021).
- [28] P. Tenenbaum and T. Shintake, Measurement of small electron-beam Spots, *Annu. Rev. Nucl. Part. Sci.* **49**, 125 (1999).
- [29] J. Yan, M. Oroku, Y. Yamaguchi, T. Yamanaka, Y. Kamiya, T. Suehara, S. Komamiya, T. Okugi, N. Terunuma, T. Tauchi, S. Araki, and J. Urakawa, Shintake Monitor Nanometer Beam Size Measurement and Beam Tuning, *Physics Procedia* **37**, 1989 (2012).
- [30] A. Seidel, J. Osterhoff, and M. Zepf, Characterizing ultralow emittance electron beams using structured light fields, *Phys. Rev. Accel. Beams* **24**, 012803 (2021).
- [31] F. C. Salgado, A. Kozan, D. Seipt, D. Hollatz, P. Hilz, M. Kaluza, A. Sävert, A. Seidel, D. Ullmann, Y. Zhao, and M. Zepf, All-optical source size and emittance measurements of laser-accelerated electron beams, *Phys. Rev. Accel. Beams* **27**, 052803 (2024).
- [32] S. Fritzler, E. Lefebvre, V. Malka, F. Burgy, A. E. D’Angor, K. Krushelnick, S. P. D. Mangles, Z. Najmudin, J.-P. Rousseau, and B. Walton, Emittance measurements of a laser-wakefield-accelerated electron beam, *Phys. Rev. Lett.* **92**, 165006 (2004).
- [33] E. Brunetti, R. P. Shanks, G. G. Manahan, M. R. Islam, B. Ersfeld, M. P. Anania, S. Cipiccia, R. C. Issac, G. Raj, G. Vieux, G. H. Welsh, S. M. Wiggins, and D. A. Jaroszynski, Low emittance, high brilliance relativistic electron beams from a laser-plasma accelerator, *Phys. Rev. Lett.* **105**, 215007 (2010).
- [34] J. Rosenzweig, N. Barov, S. Hartman, M. Hogan, S. Park, C. Pellegrini, G. Travish, R. Zhang, P. Davis, G. Hairapetian, and C. Joshi, Initial measurements of the UCLA rf photoinjector, *Nucl. Instrum. Methods Phys. Res., Sect. A* **341**, 379 (1994).
- [35] R. Ganter, B. Beutner, S. Binder, H. H. Braun, T. Garvey, C. Gough, C. Hauri, R. Ischebeck, S. Ivkovic, F. Le Pimpec, K. Li, M. L. Paraliyev, M. Pedrozzi, T. Schietinger, B. Steffen, A. Trisorio, and A. Wrulich, Electron beam characterization of a combined diode rf electron gun, *Phys. Rev. Spec. Top. Accel Beams* **13**, 093502 (2010).
- [36] S. G. Anderson, J. B. Rosenzweig, G. P. LeSage, and J. K. Crane, Space-charge effects in high brightness electron beam emittance measurements, *Phys. Rev. Spec. Top. Accel Beams* **5**, 014201 (2002).
- [37] O. Apsimon, B. Williamson, and G. Xia, A numerical approach to designing a versatile pepper-pot mask for emittance measurement, *Nucl. Instrum. Methods Phys. Res., Sect. A* **943**, 162485 (2019).
- [38] K. Abrahamyan, J. Bähr, I. Bohnet, M. Krasilnikov, D. Lipka, V. Miltchev, A. Oppelt, and F. Stephan, Transverse emittance measurements at the photo injector test facility at DESY Zeuthen (PITZ), in *Proceedings DIPAC* (Mainz, Germany, 2003).
- [39] J. P. Couperus, R. Pausch, A. Köhler, O. Zarini, J. M. Krämer, M. Garten, A. Huebl, R. Gebhardt, U. Helbig, S. Bock, K. Zeil, A. Debus, M. Bussmann, U. Schramm, and A. Irman, Demonstration of a beam loaded nanocoulomb-class laser wakefield accelerator, *Nat. Commun.* **8**, 487 (2017).
- [40] Y. F. Li, D. Z. Li, K. Huang, M. Z. Tao, M. H. Li, J. R. Zhao, Y. Ma, X. Guo, J. G. Wang, M. Chen, N. Hafz, J. Zhang, and L. M. Chen, Generation of 20 kA electron beam from a laser wakefield accelerator, *Phys. Plasma* **24**, 023108 (2017).
- [41] H. Wiedemann, *Particle Accelerator Physics*, 4th ed., Graduate Texts in Physics (Springer International Publishing and Imprint: Springer, 2015).
- [42] P. Antici, A. Bacci, C. Benedetti, E. Chiadroni, M. Ferrario, A. R. Rossi, L. Lancia, M. Migliorati, A. Mostacci, L. Palumbo, and L. Serafini, Laser-driven electron beam-lines generated by coupling laser-plasma sources with conventional transport systems, *J. Appl. Phys.* **112**, 044902 (2012).
- [43] M. Migliorati, A. Bacci, C. Benedetti, E. Chiadroni, M. Ferrario, A. Mostacci, L. Palumbo, A. R. Rossi, L. Serafini, and P. Antici, Intrinsic normalized emittance growth in laser-driven electron accelerators, *Phys. Rev. ST Accel. Beams* **16**, 011302 (2013).
- [44] M. Zhang, Emittance formula for slits and pepper-pot measurement, Fermilab-TM-1988 [10.2172/395453](https://arxiv.org/abs/10.2172/395453) (1996).
- [45] S. Agostinelli, J. Allison, K. Amako, J. Apostolakis, H. Araujo, P. Arce, M. Asai, D. Axen, S. Banerjee, G. Barrand, F. Behner, L. Bellagamba, J. Boudreau, L. Broglia, A. Brunengo, H. Burkhardt, S. Chauvie, J. Chuma, R. Chytrcek, G. Cooperman, G. Cosmo, P. Degtyarenko, A. Dell’Acqua, G. Depaola, D. Dietrich, R. Enami, A. Feliciello, C. Ferguson, H. Fesefeldt, G. Folger, F. Foppiano, A. Forti, S. Garelli, S. Gi-

- ani, R. Giannitrapani, D. Gibin, J. J. Gómez Cadenas, I. González, G. Gracia Abril, G. Greeniaus, W. Greiner, V. Grichine, A. Grossheim, S. Guatelli, P. Gumplinger, R. Hamatsu, K. Hashimoto, H. Hasui, A. Heikkinen, A. Howard, V. Ivanchenko, A. Johnson, F. W. Jones, J. Kallenbach, N. Kanaya, M. Kawabata, Y. Kawabata, M. Kawaguti, S. Kelner, P. Kent, A. Kimura, T. Kodama, R. Kokoulin, M. Kossov, H. Kurashige, E. Lamanna, T. Lampén, V. Lara, V. Lefebure, F. Lei, M. Liendl, W. Lockman, F. Longo, S. Magni, M. Maire, E. Medernach, K. Minamimoto, P. Mora de Freitas, Y. Morita, K. Murakami, M. Nagamatu, R. Nartallo, P. Nieminen, T. Nishimura, K. Ohtsubo, M. Okamura, S. O’Neale, Y. Oohata, K. Paech, J. Perl, A. Pfeiffer, M. G. Pia, F. Ranjard, A. Rybin, S. Sadilov, E. Di Salvo, G. Santin, T. Sasaki, N. Savvas, Y. Sawada, S. Scherer, S. Sei, V. Sirotenko, D. Smith, N. Starkov, H. Stoecker, J. Sulkimo, M. Takahata, S. Tanaka, E. Tcherniaev, E. Safai Tehrani, M. Tropeano, P. Truscott, H. Uno, L. Urban, P. Urban, M. Verderi, A. Walkden, W. Wander, H. Weber, J. P. Wellisch, T. Wenaus, D. C. Williams, D. Wright, T. Yamada, H. Yoshida, and D. Zschiesche, Geant4—a simulation toolkit, *Nucl. Instrum. Methods Phys. Res., Sect. A* **506**, 250 (2003).
- [46] J. Allison, K. Amako, J. Apostolakis, H. Araujo, P. Arce Dubois, M. Asai, G. Barrand, R. Capra, S. Chauvie, R. Chytracsek, G. Cirrone, G. Cooperman, G. Cosmo, G. Cuttone, G. G. Daquino, M. Donszelmann, M. Dressel, G. Folger, F. Foppiano, J. Generowicz, V. Grichine, S. Guatelli, P. Gumplinger, A. Heikkinen, I. Hrivnacova, A. Howard, S. Incerti, V. Ivanchenko, T. Johnson, F. Jones, T. Koi, R. Kokoulin, M. Kossov, H. Kurashige, V. Lara, S. Larsson, F. Lei, O. Link, F. Longo, M. Maire, A. Mantero, B. Mascialino, I. McLaren, P. Mendez Lorenzo, K. Minamimoto, K. Murakami, P. Nieminen, L. Pandola, S. Parlati, L. Peralta, J. Perl, A. Pfeiffer, M. G. Pia, A. Ribon, P. Rodrigues, G. Russo, S. Sadilov, G. Santin, T. Sasaki, D. Smith, N. Starkov, S. Tanaka, E. Tcherniaev, B. Tome, A. Trindade, P. Truscott, L. Urban, M. Verderi, A. Walkden, J. P. Wellisch, D. C. Williams, D. Wright, and H. Yoshida, Geant4 developments and applications, *IEEE Trans. Nucl. Sci.* **53**, 270 (2006).
- [47] J. Allison, K. Amako, J. Apostolakis, P. Arce, M. Asai, T. Aso, E. Bagli, A. Bagulya, S. Banerjee, G. Barrand, B. R. Beck, A. G. Bogdanov, D. Brandt, J. Brown, H. Burkhardt, P. Canal, D. Cano-Ott, S. Chauvie, K. Cho, G. Cirrone, G. Cooperman, M. A. Cortés-Giraldo, G. Cosmo, G. Cuttone, G. Depaola, L. Desorgher, X. Dong, A. Dotti, v.d. Elvira, G. Folger, Z. Francis, A. Galoyan, L. Garnier, M. Gayer, K. L. Genser, V. M. Grichine, S. Guatelli, P. Guèye, P. Gumplinger, A. S. Howard, I. Hrivnáčová, S. Hwang, S. Incerti, A. Ivanchenko, V. N. Ivanchenko, F. W. Jones, S. Y. Jun, P. Kaitaniemi, N. Karakatsanis, M. Karamitros, M. Kelsey, A. Kimura, T. Koi, H. Kurashige, A. Lechner, S. B. Lee, F. Longo, M. Maire, D. Mancusi, A. Mantero, E. Mendoza, B. Morgan, K. Murakami, T. Nikitina, L. Pandola, P. Paprocki, J. Perl, I. Petrović, M. G. Pia, W. Pokorski, J. M. Quesada, M. Raine, M. A. Reis, A. Ribon, A. Ristić Fira, F. Romano, G. Russo, G. Santin, T. Sasaki, D. Sawkey, J. I. Shin, I. I. Strakovsky, A. Taborda, S. Tanaka, B. Tomé, T. Toshito, H. N. Tran, P. R. Truscott, L. Urban, V. Uzhinsky, J. M. Verbeke, M. Verderi, B. L. Wendt, H. Wenzel, D. H. Wright, D. M. Wright, T. Yamashita, J. Yarba, and H. Yoshida, Recent developments in Geant4, *Nucl. Instrum. Methods Phys. Res., Sect. A* **835**, 186 (2016).
- [48] Y.-W. Chen, R. Kodama, and Z. Nakao, Penumbra imaging of laser-imploded targets and its blind reconstruction, *IEEE Trans. Nucl. Sci.* **45**, 992 (1998).
- [49] S. S. Haykin, *Blind deconvolution*, Prentice Hall information and system sciences series (PTR Prentice Hall, 1994).
- [50] N. Delerue, R. Bartolini, G. Doucas, P. Lau, K. Peach, A. Reichold, R. Senanayake, and D. Urner, Single-shot emittance measurement of a 508MeV electron beam using the pepper-pot method, in *Proceedings of the 23rd Particle Accelerator Conference* (Joint Accelerator Conferences Website (JACoW), 2009) pp. 3597–3599.
- [51] S. Kuschel, M. B. Schwab, M. Yeung, D. Hollatz, A. Seidel, W. Ziegler, A. Sävert, M. C. Kaluza, and M. Zepf, Controlling the Self-Injection Threshold in Laser Wakefield Accelerators, *Phys. Rev. Lett.* **121**, 154801 (2018).
- [52] NIST, *ESTAR database* (2022), accessed: 07. Nov. 2022.
- [53] Oxford Instruments, *Marana sCMOS - Andor* (2022), accessed: 07. Nov. 2022.
- [54] B. Hidding, G. Pretzler, J. B. Rosenzweig, T. Königstein, D. Schiller, and D. L. Bruhwiler, Ultracold electron bunch generation via plasma photocathode emission and acceleration in a beam-driven plasma blowout, *Phys. Rev. Lett.* **108**, 035001 (2012).